Check for updates

Directional Polarized Light Emission from Thin-Film Light-Emitting Diodes

Xiangyu Fu, Yash Mehta, Yi-An Chen, Lei Lei, Liping Zhu, Nilesh Barange, Qi Dong, Shichen Yin, Juliana Mendes, Siliang He, Renuka Gogusetti, Chih-Hao Chang, and Franky So*

Light-emitting diodes (LEDs) with directional and polarized light emission have many photonic applications, and beam shaping of these devices is fundamentally challenging because they are Lambertian light sources. In this work, using organic and perovskite LEDs (PeLEDs) for demonstrations, by selectively diffracting the transverse electric (TE) waveguide mode while suppressing other optical modes in a nanostructured LED, the authors first demonstrate highly directional light emission from a full-area organic LED with a small divergence angle less than 3° and a TE to transverse magnetic (TM) polarization extinction ratio of 13. The highly selective diffraction of only the TE waveguide mode is possible due to the planarization of the device stack by thermal evaporation and solution processing. Using this strategy, directional and polarized emission from a perovskite LED having a current efficiency 2.6 times compared to the reference planar device is further demonstrated. This large enhancement in efficiency in the PeLED is attributed to a larger contribution from the TE waveguide mode resulting from the high refractive index in perovskite materials.

With the rapid growth in portable displays, thin-film light-emitting diodes (LEDs) have attracted great attention due to their low fabrication cost and high efficiency compared with inorganic LEDs and liquid crystal displays. Typical thin-film LEDs are less than two hundred nanometers in thickness, consisting of an indium tin oxide (ITO) anode, hole and electron transport layers, an emitting layer, and a metal cathode. Depending on the emitting material, thin-film LEDs can be categorized into organic LEDs (OLEDs),[1] polymer LEDs,[2] quantum dot LEDs,[3] and perovskite LEDs (PeLEDs).[4]

A thin-film LED stack forms a microcavity between a metal electrode and an ITO anode (**Figure 1**a). Usually the cavity length of the device is optimized to achieve a maximum light outcoupling efficiency, resulting in a Lambertian-like air mode emission profile due to the weak cavity effects.[5] Controlling the emission profile of a thin-film LED is desirable for many applications and is referred to as beam-shaping.[6] In particular, highly directional beam shapes lead to many interesting applications in solid-state lighting,[7] stereoscopic displays,[8] holographic displays,[9] optical communication,[10,11] and integrated lasers.[12]

In recent years, near-eye displays such as virtual reality (VR) and augmented reality (AR) have gained great momentum in various applications.[13] Despite the rapid progress, VR displays are often bulky and heavy due to the light collimating refractive lenses.[14] In contrast, some AR displays use microdisplays and waveguide optical components to project the images which leads to a smaller form factor. However, the throughput from the input-output diffractive/holographic components are only 10%, resulting in an overall outcoupling efficiency less than 2%.[15] One way to improve both AR and VR displays is to use image sources with directional light emission (**Figure 2**). This eliminates the need for a light collimator or optical combiners, thus reducing the display size while improving the outcoupling efficiency.

Several beam-shaping approaches have been demonstrated in thin-film LEDs and they have their merits and limitations. Distributed Bragg reflectors (DBRs) can significantly enhance the cavity resonance to achieve directional emission and even lasing (Figure S1a, Supporting Information).[16–20] The layered structure of DBRs is compatible with thin-film LED fabrication, but the emission direction is sensitive to the cavity length and its emission spectrum is highly angle dependent (Figure S2, Supporting Information). Alternatively, thin-film LED pixels can be made into line or point sources with microlens arrays to collimate the emitted light (Figure S1b, Supporting Information).[21] This approach has been used in white emitting OLEDs to demonstrate a small beam divergence angle of 9°,[22,23] but due to its small pixel size, the maximum brightness per area is limited and therefore this approach is not practical.

Dr. X. Fu, Y. Mehta, L. Lei, Dr. L. Zhu, Dr. N. Barange, Q. Dong, S. Yin, J. Mendes, S. He, R. Gogusetti, Prof. F. So
Department of Materials Science and Engineering
North Carolina State University
Raleigh, NC 27606, USA
E-mail: fso@ncsu.edu
Y.-A. Chen, Prof. C.-H. Chang
Walker Department of Mechanical Engineering
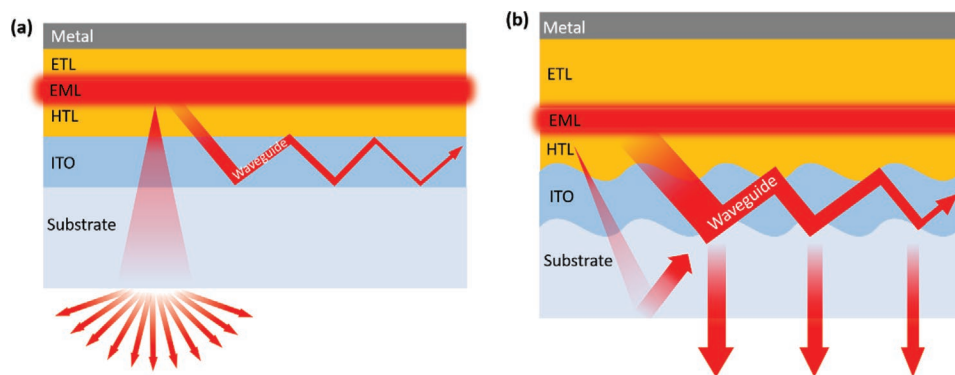University of Texas at Austin
Austin, TX 78712, USA

Figure 1. a) A conventional thin-film LED with a Lambertian air mode emission profile. b) A waveguide emission thin-film LED emitting directional light by suppressing the air mode and extracting the waveguide mode.

Instead of beam-shaping the air mode, diffractive optical elements (DOEs) have been used to extract thin-film optical modes for directional emission. Because the optical cavity length of a thin-film LED is close to the wavelength of light, it only supports the low-order transverse optical modes, which have highly quantized mode dispersions. By incorporating a DOE into a thin-film LED, the optical modes can be extracted to a narrow range of angles through Bragg diffraction (Figure S1c, Supporting Information). Zhang et al. patterned the OLED emitting layer with 2D square array of pillars, and the resulting corrugated Ag electrode diffracts the waveguide modes.[24] However, with this device, the corrugated metal cathode extracts the transverse electric (TE) waveguide mode, the transverse magnetic (TM) waveguide mode, and the surface plasmon polariton (SPP) mode, resulting in a complex emission profile with the presence of the background air mode. An alternative approach is to laterally separate the LED pixel from the DOE pixel in the device stack, such that the air mode emitted from the LED pixel can be blocked,[25] and subsequently emitted photons are coupled into a thin-film waveguide stripe and extracted by the DOE pixel, yielding directional emission (Figure S3, Supporting Information),[26] but due to the low coupling efficiency and high waveguide loss, the device efficiency is less than 1%.

Another important aspect of thin-film LEDs that is often overlooked is how to achieve polarized emission. One approach is to mechanically align the emitting molecules, resulting in polarized emission from the device.[27,28] Alternatively, a fine metallic grating is used as an external polarizer to selectively transmit the TM light and reflect the TE light.[29] However, these approaches are not practical. Uniaxial alignment inevitably induces contamination to the emission layer and damages

to the devices, and the metallic grating wastes the TE light and reduces the outcoupling efficiency by half.[30] Therefore, it is desirable to have a light source intrinsically emitting polarized light.

Herein, we demonstrate full-area highly directional polarized light emission from organic and perovskite LEDs on nanostructured substrates to selectively extract the TE waveguide mode while suppressing the SPP, TM waveguide, and air modes (Figure 1b). We first demonstrate such a device concept using an OLED with an Ir-complex emitter. By tuning the thickness of the OLED stack, the corrugation is mostly planarized at the cathode and the diffraction of TM waveguide mode and SPP mode is highly suppressed. To further suppress the emission from the air mode, the thickness of the electron transport layer (ETL) is tuned to its valley thickness in the air mode profile (Figure S4, Supporting Information) so the emission from the OLED cavity is blocked by total internal reflection from glass to air. The resulting waveguide emitting LED shows only strong TE waveguide emitted light with a high TE to TM mode extinction ratio. We then apply a similar architecture to an OLED with an Eu-complex emitter having a narrow emission spectrum to demonstrate the highly directional beam shape with a divergence angle less than 3°. Finally, we take advantage of the large index of perovskite materials and strong TE waveguide mode present in perovskite LEDs, and demonstrated directional polarized emission from such devices with a 2.6 times enhancement in current efficiency compared with the reference planar device.

To achieve waveguide-only emission in a thin-film LED, the device architecture needs to extract the waveguide mode while suppressing emission from the air, TM waveguide, and SPP
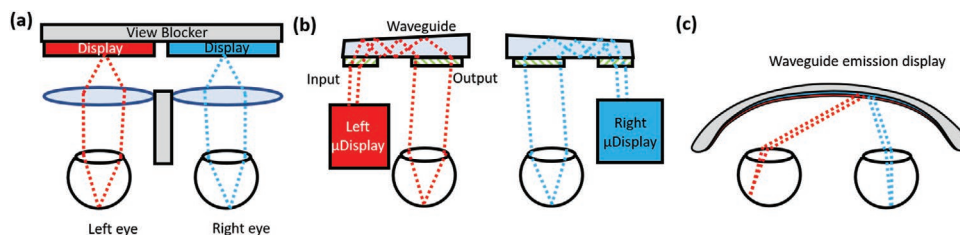

Figure 2. a,b) Schematic drawings of: a) a VR headset using refractive lenses to collimate light; and b) an AR headset using diffractive/holographic optical elements to input and output the images. c) Concept of a compact 3D display using waveguide emission display to directly project the images to the user's eyes.
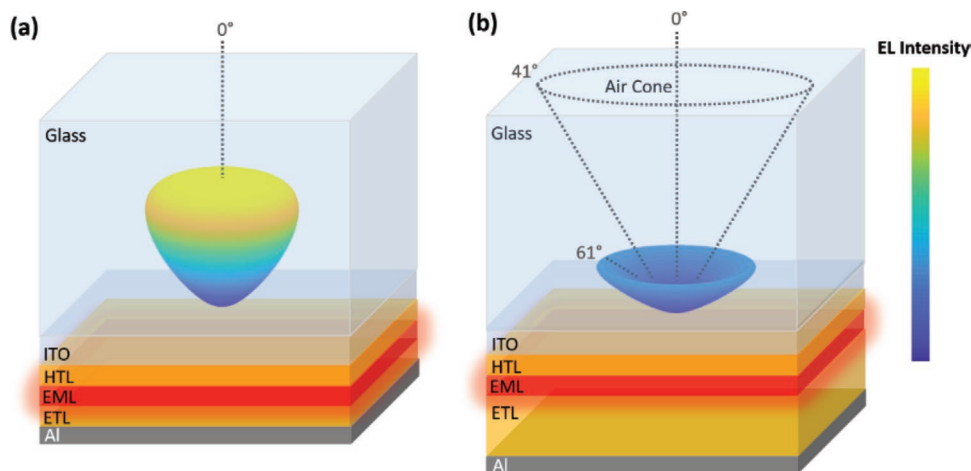
Figure 3. a,b) Simulated angular emission profile in the substrate at 60 nm ETL (maximal air mode) (a) and 140 nm ETL (minimal air mode) (b). The wavelength of the light is 520 nm, corresponding to the EL peak of Ir(ppy)$_3$.

modes. The air mode emission of a thin-film LED is determined by the cavity effect. Because the reflectivity is 85% for the Al cathode but 2% for the ITO anode, the cavity effect is mostly determined by the distance between the emitting layer (EML) and the reflective electrode, which is the thickness of the ETL in most thin-film LEDs. Herein, we use a typical OLED having a structure of glass substrate/ITO/hole transport layer (HTL)/EML/ETL/cathode to demonstrate the waveguide emission architecture. A common Ir-complex tris[2-phenylpyridinato-C^2,N]iridium(III) (Ir(ppy)$_3$) is used as the emitter, which has an EL peak at 520 nm.

To achieve pure TE waveguide emission, our first task is to suppress the emission from the air mode. Based on the optical mode distribution, the air mode intensity changes periodically with the ETL thickness (Figure S4, Supporting Information). From the peak to the valley, the air mode contribution drops from 26% to 3% while the substrate mode increases from 21% to 42%. To understand the difference in the mode distribution, we simulate the angular emission profile inside the glass substrate at the air mode peak (60 nm ETL) and valley (140 nm ETL), respectively (**Figure 3**). With a 60-nm-thick ETL, the emission profile is acorn-shaped with a strong distribution in the normal direction; therefore, light can easily escape from the

substrate, resulting in the air mode being the strongest. With a 140-nm-thick ETL, the emission profile becomes bowl-shaped, and the peak angle shifts to 61°, above the critical angle of 41° from glass to air, which results in the total internal reflection of the light and a strong reduction of the air mode. When the ETL thickness increases above 140 nm, a higher order cavity mode appears, and the air mode intensity increases again (Figure S5, Supporting Information). These simulation results indicate we can suppress the air mode emission from the thin film LED cavity by simply tuning the ETL thickness.

Next, we use optical simulation to characterize the waveguide modes in an OLED. Because the refractive index of ITO is higher than that of the organic layers and the glass substrate, it forms a slab thin-film waveguide. We use the finite-difference time-domain (FDTD) method to simulate the electric field distribution of the optical modes in an OLED with a 140 nm ETL (**Figure 4**a). The results confirm that the TE waveguide mode is located at the vicinity of the ITO anode; therefore, having a corrugated ITO anode will allow effective extraction of the TE waveguide mode by diffraction. The diffraction process is described by the Bragg equation $\vec{k} = \vec{k}_{WG} - \vec{G}$, where $\vec{k}$ and $\vec{k}_{WG}$ are the in-plane wavevectors of the diffracted and the original waveguide mode, respectively, and $\vec{G}$ is the grating
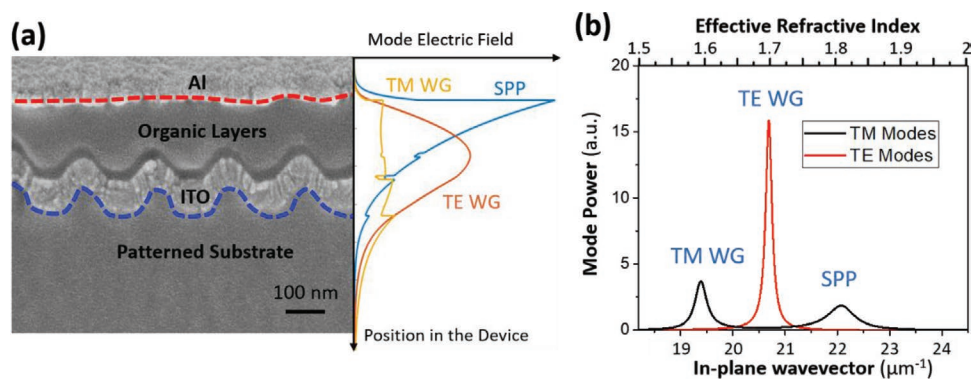

Figure 4. a) Cross-section SEM of the waveguide emission OLED fabricated on a 1D grating, and the corresponding electric field (|E|^2) distribution of the optical modes from FDTD simulation. b) The mode dispersion of a reference OLED with 140 nm ETL.
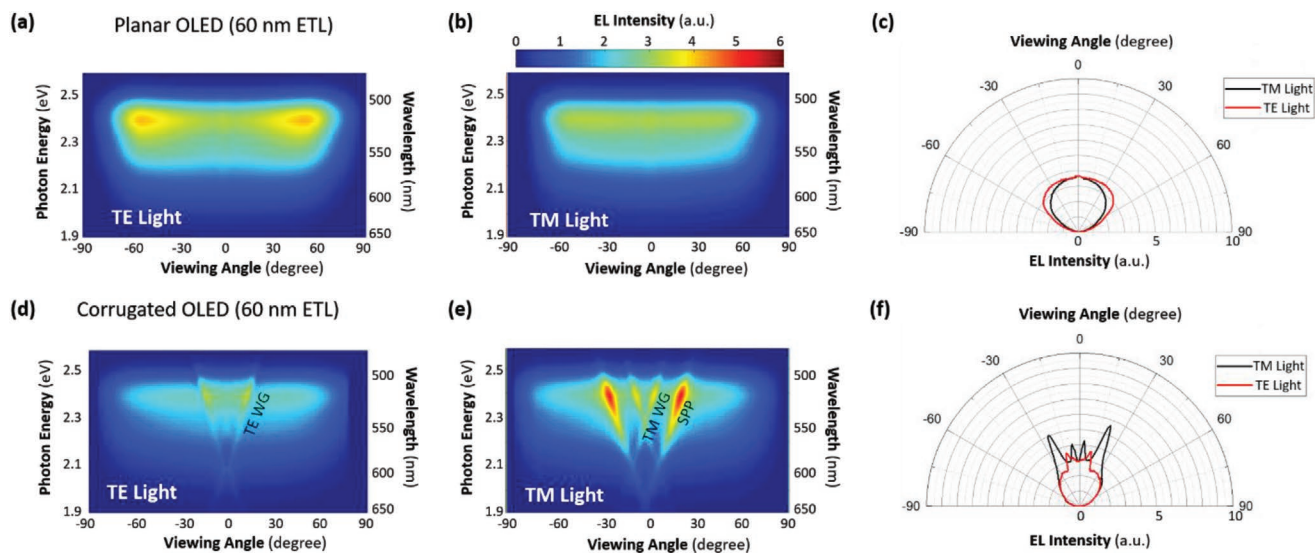
**ADVANCED
SCIENCE NEWS**

www.advancedsciencenews.com

**ADVANCED
MATERIALS**

www.advmat.de

Figure 5. a,b,d,e) Measured mode dispersion in TE and TM polarizations for a planar OLED with 60 nm ETL (a,b) and a corrugated OLED with 60 nm ETL (d,e). c,f) are the angular profiles at 520 nm for each OLED. From (d) we can see a faint feature corresponding to TE waveguide mode at 0°. This is because the corrugated substrate has larger surface area and has an overall higher film thickness than the simulated planar OLED.

vector defined by the periodicity of the corrugation Λ, such that $G = 2\pi/\Lambda$. When k is smaller than the vacuum wavevector $k_0 = 2\pi/\lambda$, the waveguide mode is extracted into air at the angle of $\theta = \sin^{-1}(k/k_0)$. Figure 4b shows the mode dispersion of the OLED device. Because the TE waveguide mode is confined in the low-loss ITO anode, it has a narrow dispersion peak, which translates to a small divergence angle from the waveguide emission OLED (Figure S6, Supporting Information).

It is important to note that in addition to the TE waveguide mode, there are one TM waveguide mode and one SPP mode present in the simulated OLED. To achieve a strongly directional and polarized emission, we need to extract the TE waveguide mode while suppressing the emission from the air, TM waveguide, and SPP modes. To suppress the air mode, the thickness of the ETL should be 140 nm, which corresponds to the air mode valley in the optical mode profile plot. In a conventional OLED where the air mode is optimized, the ETL thickness should be about 60 nm, which corresponds to the air mode maximum. Typically, having such a thin ETL in a corrugated OLED will also result in a corrugation in the Al electrode, which will diffract the SPP as well as the TM waveguide mode, as these modes have strong distribution at the metal interface. On the other hand, since we need to have a thick ETL to suppress the air mode, this thermally evaporated thick ETL will render the top cathode to be almost planarized (Figure 4a).[31] As a result, the diffraction of both the TM waveguide and SPP modes is strongly suppressed. The residual corrugation depth is not sufficient to extract the TM modes, as they have shorter propagation length due to the absorption from the metal. Further, the planarized cathode also ensures the cavity effect is preserved such that the background emission can be efficiently suppressed by increasing the ETL thickness.

To validate our device design, we fabricate OLED devices to study the effects of both the substrate corrugation and the ETL thickness (60 vs 140 nm). The corrugated substrates are patterned by soft imprinting using a master mold which consists of 1D gratings having a 350 nm period and 100 nm depth. The modest corrugation depth ensures good conductivity on the ITO anode as well to minimize its influence on the OLED cavity (Figure S7, Supporting Information). We then sputtered ITO and evaporated the organic/metallic layers on the substrates to fabricate the OLED devices. Angle-resolved emission spectra measurements were used to characterize the air mode dispersion in both TE and TM polarizations.[32,33] For OLEDs on the 1D grating substrates, the measurement plane is normal to the grating grooves. To show the effect of beam-shaping, the air mode is tuned to show the angular emission profile at 520 nm, corresponding to the peak wavelength of the green emitter Ir(ppy)$_3$.

For the planar OLED with a 60 nm-thick ETL, we observe the typical broad air mode background (**Figure 5**a,b). The emission profile shows a Lambertian-like pattern, with similar TE and TM emission profiles (Figure 5c). With a corrugated substrate, the OLED shows additional multiple diffraction features in addition to the featureless background from the air mode (Figure 5d,e). Based on the polarization and in-plane wavevector, the diffraction features are identified as the diffracted TE waveguide mode, TM waveguide mode and SPP mode.[33] The strong TM waveguide mode and SPP mode diffraction is caused by the corrugated Al with a depth of around 60 nm, which is confirmed in the cross-section SEM image (Figure S8, Supporting Information). Due to the light scattering from the corrugated Al, the cavity effect is weakened, and the background emission is reduced. Because several optical modes are diffracted into the air mode, the emission profile of the corrugated OLED has multiple peaks in both TE and TM polarizations (Figure 5f). The two TE polarized peaks come from the diffracted TE waveguide mode propagating at opposite directions. The TM polarized peaks can be attributed to the diffracted SPP modes at ±20° and the diffracted TM waveguide modes at ±4°. The magnitude of the SPP peaks is higher than the waveguide peaks because the SPP mode percentage of a device with a 60-nm-thick ETL is higher than the waveguide
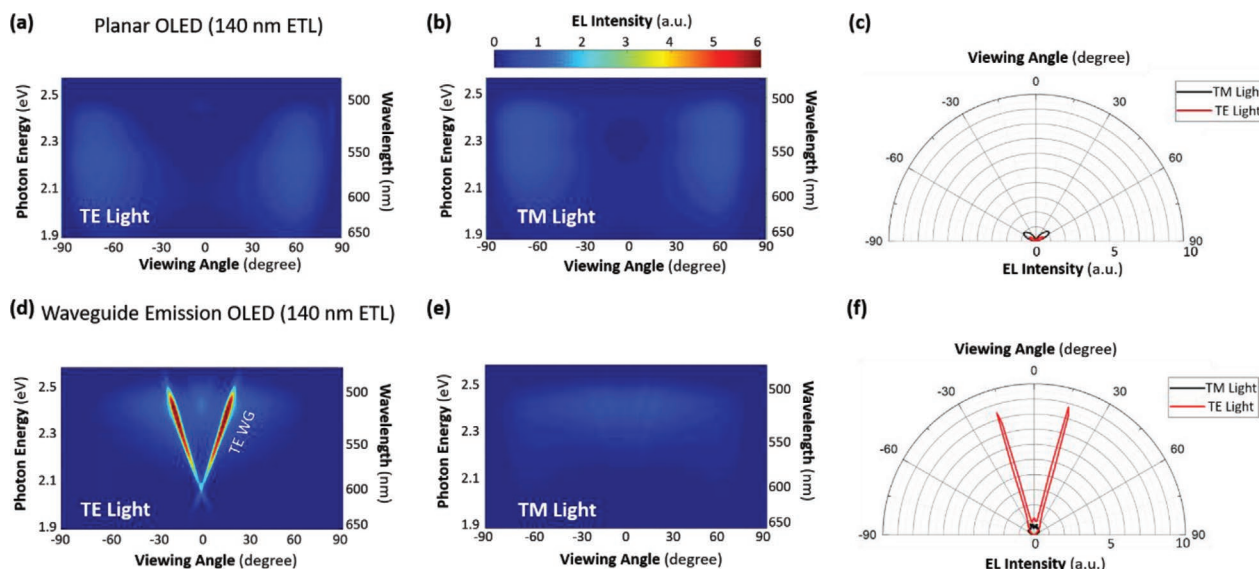
Figure 6. a,b,d,e) Measured mode dispersion in TE and TM polarizations for a planar OLED with 140 nm ETL (a,b) and a waveguide emission OLED with 140 nm ETL (d,e). c,f) The angular profiles at 520 nm for each OLED.

modes and is strongly diffracted at the highly corrugated Al cathode.

For the planar OLED with a 140 nm ETL, the measured mode dispersion is very different. Both the TE and TM polarized air modes almost completely vanished due to the suppression of the air mode emission (**Figure 6**a–c). With a corrugated substrate, the OLED still shows a negligible air mode background as expected, but with distinct TE waveguide mode diffraction features in the TE light profile. It is important to note that there are almost no TM waveguide mode or SPP mode features in the TM light profile (Figure 6d–f). The vanishing of the TM waveguide and SPP features is resulted from the 140-nm-thick ETL layer which efficiently planarized the Al cathode and suppressed the diffraction of the TM waveguide and SPP modes. From the emission profile, we can only see a highly directional emission peak corresponding to the TE waveguide emission, with a full-width at half-maximum (FWHM) divergence angle between 3.5° and 4.1°, depending on the wavelength (Figure S22, Supporting Information). Due to the effective suppression of both the air mode background and diffraction of the TM polarized

modes, the emission is highly polarized. We calculate the TE/TM extinction ratio for each wavelength at the corresponding waveguide emission peak (**Figure 7**c). A high extinction ratio of 13 is obtained between 520 and 540 nm, where the air mode emission is strongly suppressed using the cavity effect.

We compare the EQEs of the planar OLED and the waveguide emission OLED in Figure 7a. For the planar OLED having a 60-nm-thick ETL, the outcoupling efficiency is maximized and the device has an EQE of 25%. When the ETL is increased to 140 nm, the outcoupling efficiency is minimized and the EQE is reduced to 2%. By incorporating corrugation in the device to extract the TE waveguide mode, the EQE of the waveguide emission OLED is increased to 7%, indicating the TE waveguide mode emission contributes an additional 5% of the EQE. This efficiency is much lower than the 21% TE waveguide mode distribution based on the optical simulation results, which estimates to a 24% TE waveguide mode extraction efficiency (Table S1, Supporting Information). The inefficient extraction of the waveguide mode can be attributed to two factors. First, diffraction due to the grating is limited by
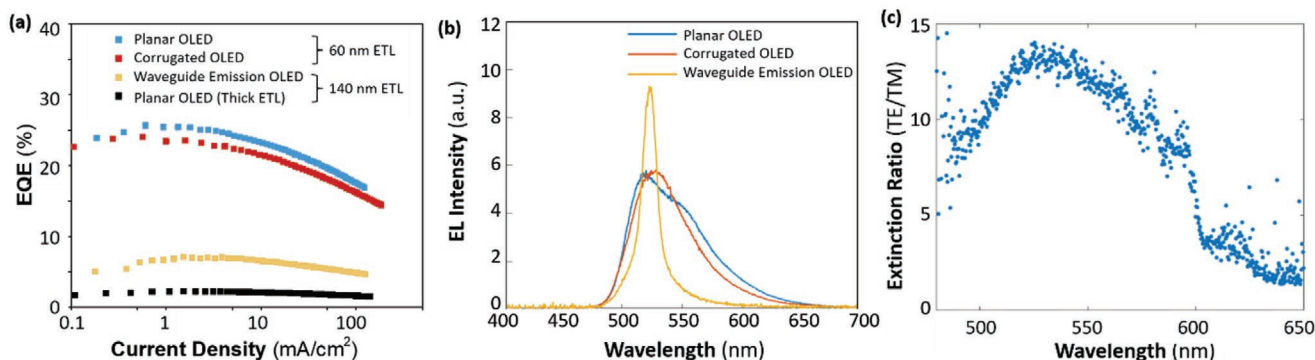

Figure 7. a,b) EQE (a) and EL (b) spectra comparison of the planar OLEDs, corrugated OLED, and waveguide emission OLED. The EL spectra are measured at 18° viewing angle where the spectrum FWHM of the waveguide emission OLED is the smallest. c) The extinction ratio of the waveguide emission OLED at each wavelength.
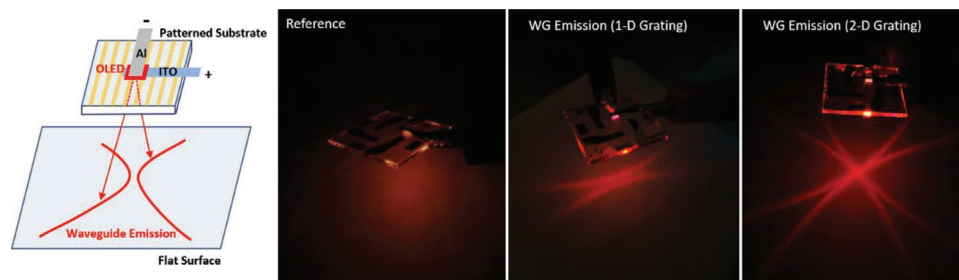
Figure 8. Spatial pattern from a reference OLED, a waveguide (WG) emission OLED on a 1D grating substrate, and a waveguide emission OLED on a 2D square grating substrate, using a narrow spectrum Eu-complex emitter. All devices are driven at 12.5 mA cm^{-2}.

the shallow corrugation depth of 100 nm and the small index contrast between the ITO and grating. Second, the propagation length of the TE waveguide mode is limited by the residual optical absorption from ITO, Al, and grating, which limits the chance of diffraction. There are two approaches to improve the extraction efficiency of the TE waveguide mode. First, we can reduce the absorption with a more reflective Ag top electrode. Second, we can improve the corrugation geometry and the index contrast of the grating, which requires further optimization of the grating design and fabrication.

In addition to the directionality and polarization, the waveguide emission OLED also shows stronger EL peak intensity and smaller FWHM (Figure 7b). At 18° viewing angle, the EL peak of the waveguide emission OLED is 1.6 times higher than the reference OLED, while the FWHM is only 20 nm, much narrower than the planar OLED, which has a 65 nm wide emission peak. In comparison, the corrugated OLED with a 60 nm ETL has a similar FWHM as the planar OLED because of the strong air mode emission. The smaller FWHM in a waveguide emission OLED stems from the narrow dispersion of the TE waveguide mode, which is confined in the low-loss 110-nm-thick ITO anode (Figure 4b). In Figure S9, Supporting Information, we plot the normalized air mode dispersion of the Ir-complex waveguide emission OLED, which eliminated the influence of the emitter spectrum and reveals the line-shape of the TE waveguide mode.[34] The spectral width of the extracted TE waveguide mode is 18 nm, much narrower than the spectral width of Ir(ppy)$_3$; therefore, the FWHM of the emitted light is significantly reduced. However, it also means a large portion of the emitter spectrum does not contribute to the waveguide emission at a given angle. As a result, the luminance of the waveguide emission OLED, which is a convolution of the EL spectra with the luminosity function, is actually lower than the planar OLED.

So far, we have demonstrated waveguide emission with a broad-spectrum emitter Ir(ppy)$_3$. Due to dispersion of the air and waveguide mode, the waveguide emission angle is different for each wavelength; therefore, we cannot realize the directional emission spatially (Figure S10, Supporting Information). To visualize the directional waveguide emission, we use an europium (Eu) complex Tris(dibenzoylmethane) mono(1,10-phenanthroline)europium(lll) (Eu(dbm)$_3$(phen)) as the emitter, which has a narrow FWHM of 4 nm (Figure S11, Supporting Information).[35] This drastically reduces the divergence caused by dispersion and allows us to visualize the spatial pattern from the waveguide emission. We also include a 2D square grating substrate to demonstrate the effect of the DOE on the spatial

pattern. The 2D grating has the same lattice constant of 350 nm as the 1D grating (Figure S12, Supporting Information).

We fabricated Eu-complex-based OLEDs on a planar substrate, a 1D grating substrate, and a 2D square grating substrate. All three OLEDs have the same pixel size of 2 mm × 2 mm. To minimize the background emission near the Eu-complex emission peak at 612 nm, we made a small adjustment to the OLED structure and increased the ETL thickness to 170 nm. We compare the emission pattern cast from the OLEDs onto a flat surface (**Figure 8**). For the planar OLED, the pattern is broad and featureless due to the Lambertian profile. For the waveguide emission OLED on a 1D grating substrate, we observe two bright arcs, corresponding to the two counter-propagating TE waveguide modes diffracted by the grating. Different points on the arcs originate from the TE waveguide modes propagating at different in-plane directions, which are explained using the reciprocal space (Figure S13, Supporting Information). For the waveguide emission OLED on a 2D square grating substrate, we observe a cross pattern consisting of four arcs. This is because a square lattice defines two orthogonal sets of $\vec{G}$; therefore, the TE waveguide mode is diffracted in the two orthogonal directions. Note that a gap can be observed between the arcs with the 1D grating substrate but are not observed with the 2D grating substrate. The reason is that the 2D grating substrate has lower fill factor than the 1D grating, which leads to more ITO at the corrugated interface and a larger effective refractive index of the waveguide mode (and thus the radius of the arcs), resulting in closing the gap.

We can also examine the emission pattern of a waveguide emission OLED based on its tunability and robustness. Based on the Bragg equation $\vec{k} = \vec{k}_{WG} - \vec{G}$, the spatial pattern of the waveguide emission OLED can be modified by tuning the waveguide mode $\vec{k}_{WG}$ or the DOE pattern $\vec{G}$. Because tuning $\vec{k}_{WG}$ requires changing the refractive indices of the OLED layers, it is limited by the available materials with the suitable optical and electrical properties. A more feasible way to modify the spatial pattern is using different DOEs, as has been demonstrated with the 1D and 2D patterns. In addition, the emission angle can be tuned from 1° to 19° by changing the grating periodicity from 350 to 300 nm, respectively (Figure S14, Supporting Information); with a 2D patterned substrate, the emission angles can be tuned separately for each optical axis using a dual-periodicity substrate.[36]

Once a DOE pattern is chosen, it is important for the waveguide emission pattern to have high tolerance for the variability in the OLED fabrication process. For the waveguide emission design,

the most critical parameter is the grating periodicity, which can be precisely controlled by lithography. Other parameters to consider are thicknesses of the layers, which can alter the optical cavity. One key dimension is that during thermal evaporation, the organic layer thickness could have slight variation across the panel or across each pixel (due to the shadow mask). To study the extreme cases, we vary the thicknesses of the HTL by 30 nm and the ETL by 20 nm to examine the change in the waveguide emission angle (Figures S15 and S16, Supporting Information). In both cases, the emission angle only changed by 1°, which confirms the robustness of the waveguide emission OLED design.

Using a similar approach as the Ir-complex waveguide emission OLED, we examine the spectral FWHM and the luminance profile of the Eu-complex waveguide emission OLED (Figure S17, Supporting Information). The spectral width of the TE waveguide mode is also 18 nm, much larger than the spectral FWHM of the Eu-complex emitter; hence, the spectrum narrowing effect is less noticeable. On the other hand, the broader TE waveguide mode enhances all the wavelength components of an Eu-complex emitter at the peak angle; therefore, we observed a 2× luminance enhancement in the forward luminance with a 1D grating, and 3× luminance enhancement with a 2D grating, respectively. The stronger enhancement with a 2D grating is because the four waveguide emission arcs perfectly align in the normal direction.

Although the Eu and other lanthanide complex emitters have a very narrow EL peak that is suitable for highly directional emission, they often have low quantum efficiency below 10%.[37,38] In comparison, quantum dot LEDs[39,40] and perovskite LEDs[41–43] have shown over 20% external quantum efficiency with tunable EL spectra as narrow as 20 nm, and thus are great candidates for realizing high efficiency, low chromatic dispersion waveguide emission.

Other than the intrinsic EQE, we discovered that the most important factor that determines the efficiency of the waveguide emission LED is the refractive index of the emitting material. As the refractive index of the EML increases, the TE waveguide mode percentage will be higher, which can be explained by the normalized modal electric field distribution (Figures S18 and S19, Supporting Information). To demonstrate the refractive index dependence, we simulated the optical mode percentage in a waveguide emission LED architecture with a 30-nm-thick EML as a function of the refractive index of the emission layer n(EML) between 1.5 and 2.5 (**Figure 9**). The result shows that the TE waveguide mode percentage increases with n(EML). Specifically, for a perovskite emitter having a high refractive index ($n \approx 2.3$),[45] 42% of the emitted photons are coupled to the TE waveguide mode, which is two times higher than the OLED case. With a stronger TE waveguide coupling, we expect to see stronger directional emission in a waveguide emission PeLED.

We fabricated green PeLEDs on a 1D grating substrate based on quasi 2D perovskite having a composition of $(PEA)_2(FA)_3Pb_4Br_{13}$.[46] The emission peak of the perovskite material is 522 nm, and the photoluminescence (PL) spectrum FWHM is 28 nm. The period of the grating is 300 nm, which diffracts the TE_0 waveguide mode at 530 nm to the normal direction. From the spatial pattern (**Figure 10**a), we observe the planar PeLED behaves like a Lambertian emitter while the waveguide
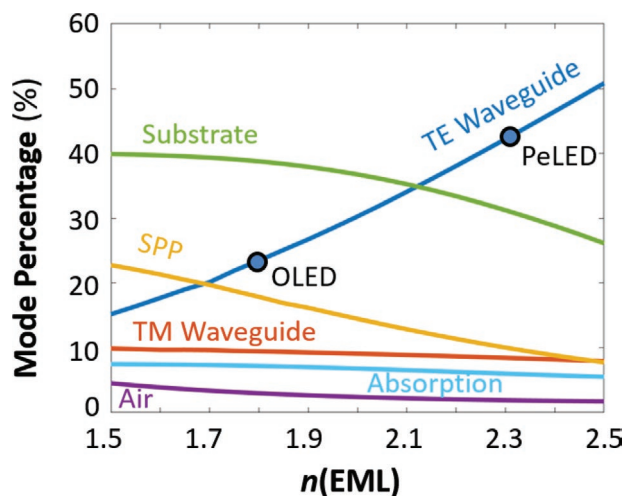

Figure 9. The dependence of optical mode percentage on the refractive index of the emitting layer in a waveguide emission thin-film LED.

emission PeLED casts two sets of arcs, originating from the diffracted TE_0 and TE_1 waveguide modes, respectively (Figure S20, Supporting Information). We note the TE_1 waveguide mode forms because the thickness of the perovskite layer is 35 nm (Figure S21, Supporting Information), which can be suppressed by reducing the ITO thickness or the EML thickness.[47] The two diffracted TE_0 arcs intersect at the normal direction, forming a strip of bright area. At each wavelength, the FWHM divergence angles of the TE_0 waveguide mode peaks are around 4° (Figure S22, Supporting Information), and the divergence angle of the integrated luminance profile is 10° near the normal direction (Figure S23, Supporting Information). As a result, the normal direction current efficiency of the waveguide emission PeLED is 56 cd A^{-1}, which is 2.6 times higher than the reference PeLED, despite the similar device EQEs (Figure 10b,c). In addition, because the intrinsic PL spectrum of the perovskite is already narrow, the color shift caused by the grating diffraction is almost unnoticeable to the eyes (Figure S23, Supporting Information). Nevertheless, the narrow perovskite EL peak width is further reduced by the waveguide emission. At 3° polar angle normal to the grating grooves, the EL peak FWHM is 12.5 nm, only half the width of a reference PeLED (Figure 10d).

We note that the modest device efficiency of the reference PeLED is due to the perovskite film with a low PL quantum yield (PLQY) of 40%. The thin perovskite film is necessary to confine the TE waveguide mode in the ITO anode, which suppresses the re-absorption from the perovskite EML and maximizes the waveguide mode extraction (Figure S24 and Table S2, Supporting Information). To date, the highest current efficiencies reported for green PeLEDs are 62.5 cd A^{-1} (PLQY = 73.8%) in a 2D perovskite system[48] and 78 cd A^{-1} (PLQY = 80%) in a 3D perovskite system.[43] With a close to 100% PLQY and a fully optimized reference green emitting PeLED, the current efficiency is expected to be higher than 80 cd A^{-1}. Using such a device to fabricate a waveguide emission PeLED, a current efficiency of 170 cd A^{-1} is possible. Such highly directional and high efficiency PeLED design paves the way for high color purity light-emitting devices for display and solid-state lighting applications.
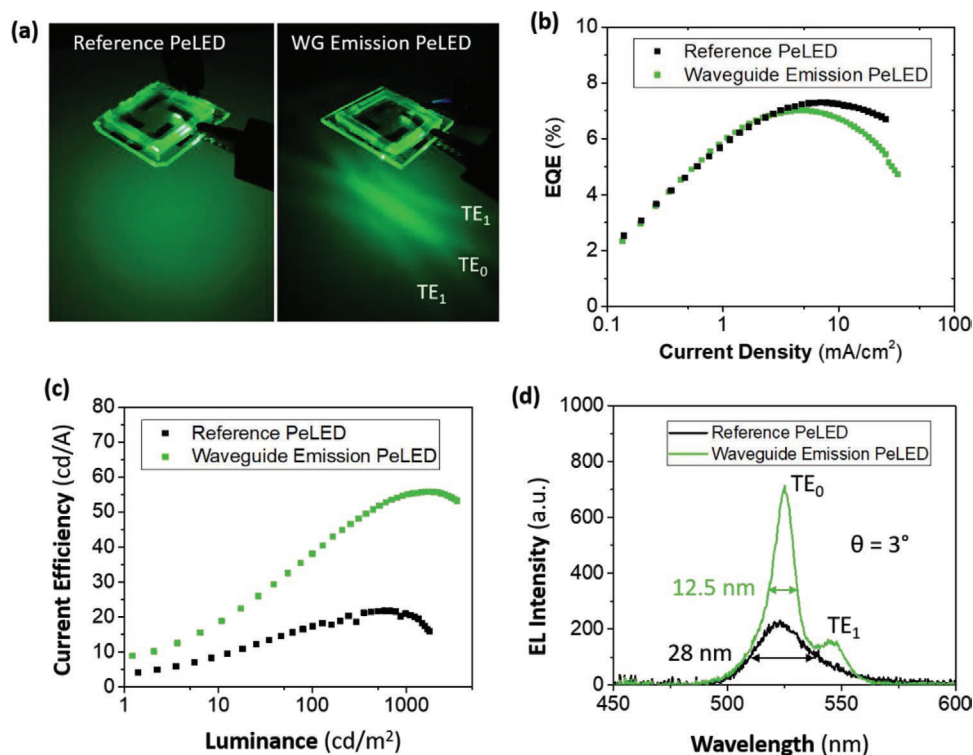
ADVANCED
SCIENCE NEWS
www.advancedsciencenews.com

ADVANCED
MATERIALS
www.advmat.de

Figure 10. a) Spatial patterns from a reference PeLED and a waveguide emission PeLED on a 1D grating substrate. Both devices are driven at 2.5 mA cm^{-2}. b,c) Comparisons of the device EQE (b) and current efficiencies (c) measured in the normal direction. d) EL spectra measured at $\theta = 3°$ normal to the grating grooves.

In summary, we designed a highly directional and polarized waveguide emission thin-film LED on a corrugated substrate such that the resulting gratings only extract the TE waveguide mode while suppressing light emission from other optical modes. To achieve these emission characteristics, the corrugation at the top cathode is planarized by thermal evaporation of a thick organic stack. This not only reduces the background air mode emission, but also suppresses the diffraction of SPP and TM waveguide modes, resulting in highly directional with a small divergence angle of 3° and polarized light emission from the TE waveguide mode having a TE/TM extinction ratio of 13. We also point out that perovskite emitters are the perfect candidates for waveguide emission due to the intrinsically high refractive index and thus high TE waveguide distribution. By extracting the TE waveguide modes into the forward direction, we demonstrate a waveguide emission perovskite LED with 2.6 times enhancement in the current efficiency. Because the device is simple to fabricate and can be easily scaled-up, our discovery of this strong directional and polarized light emission from OLEDs and perovskite LEDs has important applications for displays, lighting and other photonic applications.

Experimental Section

Fabrication of 1D and 2D Gratings: The 1D and 2D grating nanostructures on silicon substrate were patterned using a combination of interference lithography (IL)[49,50] and transferred using reactive ion etching (RIE). To begin with, a silicon substrate was spin-coated with 100 nm antireflection coating (ARC i-con-7, Brewer Science) and 180 nm positive photoresist (PFI-88A2, Sumitomo). The antireflection coating film was used to reduce the reflection from silicon substrate during interference lithography. The 1D and 2D periodic grating nanostructures in photoresist were patterned using 325 nm wavelength HeCd laser exposure in a Lloyd's mirror IL setup. Two coherent laser beams were interfered to create periodic intensity pattern in Lloyd's mirror IL setup. Then, the periodic grating pattern was transferred to the underlying silicon substrate using O_2 and Cl_2 RIE. After etching, an RCA cleaning process was used to remove the organic contaminants on the substrate surface. The surfaces of the molds were then treated with silane to mitigate adhesion for the subsequent soft-imprinting process.

Fabrication of Waveguide Emission OLEDs: For the waveguide emission OLEDs, a corrugated substrate was first fabricated through soft-imprinting. A poly(dimethylsiloxane) (PDMS) stamp was used to replicate the pattern from the master mold. The glass substrates were cleaned with standard ultrasonication procedure in acetone and isopropyl alcohol for 15 min each. Then a small amount of NOA-81 epoxy (from Norland Products Inc.) was dropcast on the glass substrate. The stamp was pressed on the epoxy to remove air gaps in between. Then the substrate with stamp was treated under 365 nm UV light (Jelight UVO cleaner Model 42) for 4 min to cure the epoxy. Afterward, the stamp was removed to leave behind the corrugated substrate.

For the Ir-complex based OLED, the device structure was ITO (110 nm)/MoO$_x$ (10 nm)/4,4′-cyclohexylidenebis[N,N-bis(4-methylphenyl)benzenamine] (TAPC) (40 nm)/4,4′-bis(N-carbazolyl)-1,1′-biphenyl (CBP) (20 nm):5% Tris[2-phenylpyridinato-C2,N]iridium(III) (Ir(ppy)$_3$)/4,7-diphenyl-1,10-phenanthroline (Bphen) (60 nm)/Bphen:12% Cs$_2$CO$_3$ (80 nm)/Cs$_2$CO$_3$ (2 nm)/Al (100 nm). Because a thick ETL was used in the waveguide emission OLED, the Cs$_2$CO$_3$ was doped in the Bphen layer to enhance the electron transport and maintain a good charge balance.[51] The reference Ir-based OLED had a similar structure, with only 60 nm Bphen as the ETL. For the Eu-complex based waveguide emission

OLED, the structure was ITO (110 nm)/MoO$_x$(10 nm)/TAPC (60 nm)/ CBP (20 nm): 10% Tris(dibenzoylmethane) mono(1,10-phenanthroline) europium(lll) (Eu(dbm)$_3$(phen))/Bphen (65 nm)/Bphen: 12% Cs$_2$CO$_3$ (105 nm)/Cs$_2$CO$_3$ (2 nm)/Al (100 nm). The reference Eu-based OLED had a similar structure, with only 65 nm Bphen as the ETL.

Fabrication of Perovskite LEDs: The materials used for the PeLEDs, formamidinium bromide (FABr), lead bromide (PbBr$_2$), methylammonium chloride (MACl), anhydrous *N*-methyl-2-pyrrolidone (NMP), and chlorobenzene were purchased from Sigma-Aldrich. Phenethylammonium bromide (PEABr) was purchased from Greatcell Solar. For the preparation of the perovskite, PEABr, FABr, PbBr$_2$ (2:3:4 molar ratio) were dissolved in 1 mL anhydrous NMP to make 0.25 M (Pb^{2+} concentration) solution, and 1 mol% MACl was added. The solution was stirred for 2 h at 60 °C in a glovebox with a nitrogen environment. For the reference and waveguide emission PeLED, the pre-patterned ITO substrates were UV-ozone treated for 15 min. PEDOT:PSS (4083) was spin-coated at 4000 rpm for 40 s and annealed at 150 °C for 15 min. Thereafter, the perovskite solution was spin-coated at 3000 rpm for 2 min, during which time (at 26 s for NMP) chlorobenzene (150 µL) was dripped onto the surface, followed by annealing at 90 °C for 10 min. The as-prepared substrates were then transferred into a thermal evaporator, and 40 nm TPBi, 2 nm Cs$_2$CO$_3$, and 100 nm Al were deposited layer by layer. For the waveguide emission PeLED, the ETL was TPBi (40 nm)/ Bphen: 10% Cs$_2$CO$_3$ (90 nm). Finally, the fabricated devices were sealed in glovebox by ultraviolet-curable resin before testing.

Characterization of OLEDs and PeLEDs: The device voltage–current density curves were measured using a Keithley 2400 SourceMeter. The EQE was measured in an integration sphere (Labsphere Illumia). The edge of the substrate was covered to block the substrate mode leakage. The current efficiency was measured with an LS-100 luminance meter. For the angle-resolved EL spectra (ARES) measurements, a spectral goniometer was set up using an automatic rotary stage (Griffin Motion, RTS-DD-100). Light from the operating device was collected and sent to the spectrometer (Ocean Optics HR4000) by an optical fiber (Thorlabs Ø200 µm, 0.22 NA) from 20 cm away. A wire grid polarizer (Thorlabs WP25L-VIS) was used to measure TE and TM light, respectively. For full-angle (−90° to 90°) measurements, the angle step was 1°. To determine the divergence angle FWHM, a finer angle step of 0.2° was used within a smaller angle range. A schematic drawing of the ARES setup is shown in Figure S25, Supporting Information.

Supporting Information

Supporting Information is available from the Wiley Online Library or from the author.

Conflict of Interest

The authors declare no conflict of interest.

[1] H. W. Chen, J. H. Lee, B. Y. Lin, S. Chen, S. T. Wu, *Light Sci. Appl.* **2018**, *7*, 17168.
[2] H. Zheng, Y. Zheng, N. Liu, N. Ai, Q. Wang, S. Wu, J. Zhou, D. Hu, S. Yu, S. Han, W. Xu, *Nat. Commun.* **2013**, *4*, 1971.
[3] Y. Shirasaki, G. J. Supran, M. G. Bawendi, V. Bulović, *Nat. Photonics* **2013**, *7*, 13.
[4] Y. H. Kim, H. Cho, J. H. Heo, T. S. Kim, N. Myoung, C. L. Lee, S. H. Im, T. W. Lee, *Adv. Mater.* **2015**, *27*, 1248.
[5] J. Lee, N. Chopra, F. So, *App. Phys. Lett.* **2008**, *92*, 19.
[6] F. Fries, M. Fröbel, P. Y. Ang, S. Lenk, S. Reineke, *Light Sci. Appl.* **2018**, *7*, 18.
[7] S. Reineke, M. Thomschke, B. Lüssem, K. Leo, *Rev. Mod. Phys.* **2013**, *85*, 1245.
[8] D. Fattal, Z. Peng, T. Tran, S. Vo, M. Fiorentino, J. Brug, R. G. Beausoleil, *Nature* **2013**, *495*, 348.
[9] S. Tay, P. A. Blanche, R. Voorakaranam, A. V. Tunç, W. Lin, S. Rokutanda, T. Gu, D. Flores, P. Wang, G. Li, P. St Hilaire, *Nature* **2008**, *451*, 694.
[10] H. Elgala, R. Mesleh, H. Haas, *IEEE Commun. Mag.* **2001**, *49*, 56.
[11] P. A. Haigh, Z. Ghassemlooy, S. Rajbhandari, I. Papakonstantinou, *IEEE Commun. Mag.* **2013**, *51*, 148.
[12] A. S. Sandanayaka, T. Matsushima, F. Bencheikh, S. Terakawa, W. J. Potscavage, C. Qin, T. Fujihara, K. Goushi, J. Ribierre, C. Adachi, *Appl. Phys. Express* **2019**, *12*, 061010.
[13] P. Cipresso, I. A. C. Giglioli, M. A. Raya, G. Riva, *Front. Psychol.* **2018**, *9*, 2086.
[14] A. Maimone, J. Wang, *ACM Trans. Graph.* **2020**, *39*, 67.
[15] Y. H. Lee, T. Zhan, S. T. Wu, *Virtual Reality Intell. Hardware* **2019**, *1*, 10.
[16] M. Wang, J. Lin, Y. Hsiao, X. Liu, B. Hu, *Nat. Commun.* **2019**, *10*, 1614.
[17] C. Murawski, A. Mischok, J. Booth, J. D. Kumar, E. Archer, L. Tropf, C. Keum, Y. Deng, K. Yoshida, I. D. W. Samuel, M. Schubert, *Adv. Mater.* **2019**, *31*, 1903599.
[18] M. Koschorreck, R. Gehlhaar, V. G. Lyssenko, M. Swoboda, M. Hoffmann, K. Leo, *App. Phys. Lett.* **2005**, *87*, 181108.
[19] A. Genco, S. Carallo, G. Accorsi, Y. Duan, S. Gambino, M. Mazzeo, *Org. Electron.* **2018**, *62*, 174.
[20] S. Meister, R. Brückner, M. Sudzius, H. Fröb, K. Leo, *Appl. Phys. Lett.* **2018**, *112*, 113301.
[21] G. L. Bai, J. J. Yang, S. X. Wu, X. X. Ma, Y. L. Ma, L. Zhou, C. B. Li, S. Shen, *Appl. Phys. Express* **2018**, *11*, 072101.
[22] S. Aratani, M. Adachi, M. Shimizu, T. Sugita, T. Shibasaki, K. Shimazaki, *Jpn. J. Appl. Phys.* **2010**, *49*, 042101.
[23] L. Zhou, G. L. Bai, X. Guo, S. Shen, Q. D. Ou, Y. Y. Fan, *Appl. Phys. Lett.* **2018**, *112*, 201902.
[24] S. Zhang, G. A. Turnbull, I. D. W. Samuel, *Appl. Phys. Lett.* **2013**, *103*, 217.
[25] S. Zhang, G. A. Turnbull, I. D. W. Samuel, *Adv. Opt. Mater.* **2014**, *2*, 343.
[26] M. Ramuz, L. Bürgi, R. Stanley, C. Winnewisser, *J. Appl. Phys.* **2009**, *105*, 084508.
[27] M. Misaki, Y. Ueda, S. Nagamatsu, M. Chikamatsu, Y. Yoshida, N. Tanigaki, K. Yase, *Appl. Phys. Lett.* **2005**, *87*, 243503.
[28] G. J. Choi, Q. Van Le, K. S. Choi, K. C. Kwon, H. W. Jang, J. S. Gwag, S. Y. Kim, *Adv. Mater.* **2017**, *29*, 1702598.
[29] M. Y. Lin, H. H. Chen, K. H. Hsu, Y. H. Huang, Y. J. Chen, H. Y. Lin, Y. K. Wu, L. A. Wang, C. C. Wu, S. C. Lee, *IEEE Photonics Technol. Lett.* **2013**, *25*, 1321.
[30] L. Zhou, Y. Zhou, B. L. Fan, F. Nan, G. H. Zhou, Y. Y. Fan, W. J. Zhang, Q. D. Ou, *Laser Photonics Rev.* **2020**, 1900341.
[31] P. A. Will, M. Schmidt, K. Eckhardt, F. Wisser, S. Lenk, J. Grothe, S. Kaskel, S. Reineke, *Adv. Func. Mater.* **2019**, *29*, 1901748.
[32] J. J. Wierer, A. David, M. M. Megens, *Nat. Photonics* **2009**, *3*, 163.
[33] T. Schwab, C. Fuchs, R. Scholz, A. Zakhidov, K. Leo, M. C. Gather, *Opt. Express* **2014**, *22*, 7524.

[34] X. Fu, C. Peng, M. Samal, N. Barange, Y.-A. Chen, D.-H. Shin, Y. Mehta, A. Rozelle, C.-H. Chang, *ACS Appl. Electron. Mater.* **2020**, *2*, 1759.

[35] J. G. Bunzli, S. Comby, A. Chauvin, C. D. B. Vandevyver, *J. Rare Earth* **2007**, *25*, 257.

[36] Y. G. Bi, J. Feng, Y. F. Li, X. L. Zhang, Y. F. Liu, Y. Jin, H. B. Sun, *Adv. Mater* **2013**, *25*, 6969.

[37] T. W. Canzler, J. Kido, *Org. Electron.* **2006**, *7*, 29.

[38] S. Zhang, G. A. Turnbull, I. D. W. Samuel, *Org. Electron* **2012**, *13*, 3091.

[39] Y. Yang, Y. Zheng, W. Cao, A. Titov, J. Hyvonen, J. R. Manders, J. Xue, P. H. Holloway, L. Qian, *Nat. Photonics* **2015**, *9*, 259.

[40] B. S. Mashford, M. Stevenson, Z. Popovic, C. Hamilton, Z. Zhou, C. Breen, J. Steckel, V. Bulovic, M. Bawendi, S. Coe-Sullivan, P. T. Kazlas, *Nat. Photonics* **2013**, *7*, 407.

[41] B. Zhao, S. Bai, V. Kim, R. Lamboll, R. Shivanna, F. Auras, J. M. Richter, L. Yang, L. Dai, M. Alsari, X. She, *Nat. Photonics* **2018**, *12*, 783.

[42] W. Xu, Q. Hu, S. Bai, C. Bao, Y. Miao, Z. Yuan, T. Borzda, A. J. Barker, E. Tyukalova, Z. Hu, M. Kawecki, *Nat. Photonics* **2019**, *13*, 418.

[43] K. Lin, J. Xing, L. N. Quan, F. P. G. De Arquer, X. Gong, J. Lu, L. Xie, W. Zhao, D. Zhang, C. Yan, W. Li, *Nature* **2018**, *562*, 245.

[44] J. D. Joannopoulos, S. G. Johnson, J. N. Winn, R. D. Meade, *Photonic Crystals: Molding the Flow of Light*, Princeton University Press, Princeton, NJ, USA **2008**.

[45] L. Zhao, K. M. Lee, K. Roh, S. Uz, Z. Khan, B. P. Rand, *Adv. Mater.* **2019**, *31*, 1805836.

[46] L. Lei, D. Seyitliyev, S. Stuard, J. Mendes, Q. Dong, X. Fu, Y.-A. Chen, S. He, X. Yi, L. Zhu, C.-H. Chang, H. Ade, K. Gundogdu, F. So, *Adv. Mater.* **2020**, *32*, 1906571.

[47] Y. Liu, J. Cui, K. Du, H. Tian, Z. He, Q. Zhou, Z. Yang, Y. Deng, D. Chen, X. Zuo, Y. Ren, L. Wang, H. Zhu, B. Zhao, D. Di, J. Wang, R. H. Friend, Y. Jin, *Nat. Photonics* **2019**, *13*, 760.

[48] X. Yang, X. Zhang, J. Deng, Z. Chu, Q. Jiang, J. Meng, P. Wang, L. Zhang, Z. Yin, J. You, *Nat. Commun.* **2018**, *9*, 570.

[49] H. I. Smith, *Phys. E* **2001**, *11*, 104.

[50] A. Bagal, C.-H. Chang, *Opt. Lett.* **2013**, *38*, 2531.

[51] Y. Chen, X. Wei, Z. Li, Y. Liu, J. Liu, R. Wang, P. Wang, Y. Yamada-takamura, Y. Wang, *J. Mater. Chem. C* **2017**, *5*, 8400.

2006801 (10 of 10)